# Power Flow Models of Grid-Forming Inverters in Unbalanced Distribution Grids

Dingrui Li, *Graduate Student Member, IEEE*, Yu Su, *Member, IEEE*, Fred Wang, *Fellow, IEEE*, Mohammed Olama, *Senior Member, IEEE*, Ben Ollis, *Senior Member, IEEE*, and Maximiliano Ferrari, *Member, IEEE*

***Abstract*—Load unbalance in electric distribution systems is unavoidable. Unbalanced load currents will lead to negative sequence (NS) voltages that may damage electric equipment. Unbalanced power flow analysis is a common tool to detect and mitigate NS voltage issues and requires accurate models of grid components. While traditional source models are available, grid-forming (GFM) inverter models are not well developed. GFM inverters implement various control strategies, which affect their power flow models. In this article, a novel GFM inverter model considering control effects is proposed. We show that for some control methods, unbalanced system loading will lead to unbalanced terminal voltages of the GFM inverters, which are modeled through an equivalent negative sequence impedance. The proposed models are initially validated using a simple test circuit. Then, they are applied in the power flow analysis on the IEEE 13-bus and 34-bus systems to demonstrate the accuracy improvement over the state-of-the-art. Using time-domain simulations as benchmarks, we show that the proposed models reduce the calculation error of negative sequence voltages by at least 25% in unbalanced distribution systems.**

***Index Terms*—Grid-forming inverter, power flow model, unbalanced load, distribution system, microgrids.**

## I. Introduction

In a three-phase electric distribution grid, single-phase and three-phase loads are served simultaneously, and it is common for the aggregated load to be unbalanced. As a result, unbalanced currents may flow in the distribution system. Unbalanced currents will introduce unbalanced voltages that can be decomposed into the positive sequence (PS), negative sequence (NS), and zero sequence (ZS) components.

Manuscript received 16 January 2023; revised 8 May 2023; accepted 17 June 2023. Date of publication 3 July 2023; date of current version 21 February 2024. This work was supported in part by the UT-Battelle, LLC under Grant DE-AC05-00OR22725 with the U.S. Department of Energy, in part by the U.S. Department of Energy's Office of Energy Efficiency and Renewable Energy through the Solar Energy Technologies Office Award under Grant DE-EE0002243-2144. Paper no. TPWRS-00084-2023. *(Corresponding author: Yu Su.)*

Dingrui Li and Yu Su are with the Department of Electrical Engineering and Computer Science, University of Tennessee, Knoxville, TN 37996 USA (e-mail: dli35@vols.utk.edu; ysu10@vols.utk.edu).

Fred Wang is with Department of Electrical Engineering and Computer Science, The University of Tennessee, Knoxville, TN 37996 USA, and also with the Oak Ridge National Laboratory, Oak Ridge, TN 37830 USA (e-mail: f.wang@ieee.org).

Mohammed Olama, Ben Ollis, and Maximiliano Ferrari are with Oak Ridge National Laboratory, Oak Ridge, TN 37831 USA (e-mail: olamahussemm@ornl.gov; ollistb@ornl.gov; ferrarimagmf@ornl.gov).

Color versions of one or more figures in this article are available at https://doi.org/10.1109/TPWRS.2023.3290611.

Digital Object Identifier 10.1109/TPWRS.2023.3290611

NS voltages in a distribution system should be limited (e.g., to below 2%) to avoid issues for electrical equipment such as three-phase motors [1]. Potential NS voltage issues can be identified using power flow analyses and mitigation strategies such as load reallocation can be implemented. Therefore, accurate modeling of different grid components considering NS is critical for identifying NS voltage issues.

For a conventional distribution grid, the modeling of different components (sources, loads, distribution lines, etc.) is well-established [2]. However, due to the increased integration of distributed energy resources (DERs), future distribution grids and microgrids will contain more inverter-based resources (IBRs) such as solar photovoltaics (PVs), battery energy storage systems, etc. [3]. Some of the interface inverters of IBRs can be operated in grid-forming (GFM) mode to provide the system with stable voltage and frequency [4], which is common in isolated grids such as microgrids and remote distribution grids. Accurate GFM inverter models are required to conduct power flow analyses in these systems. However, accurate models of GFM inverters considering unbalanced load conditions are lacking in the existing literature.

A common GFM inverter model for power flow is a controlled voltage source considering the voltage droop characteristic [5], [6], [7], [8], [9], [10], [11], [12]. This model does not consider the potential virtual impedance control or virtual synchronous generator (VSG) control, which introduces an equivalent output impedance (virtual impedance or equivalent output impedance of the generator electrical model). Moreover, under unbalanced load conditions, the impacts of the unbalanced currents flowing into the inverter on the output voltage are not considered.

Ref. [13] modeled the GFM inverter as a controlled voltage source plus its virtual impedance. However, the impacts of unbalanced currents from unbalanced loads were not considered. In order to consider unbalanced current impacts, NS models were also proposed in the power flow analysis. Refs. [14], [15], [16] proposed an impedance model for GFM inverters in NS, defined by the inverters' output filter impedance. Refs. [17], [18], [19] assumed the control loop of GFM inverters can fully compensate for the NS current impacts and used a short circuit to represent the GFM in NS. While some control strategies are able to fully compensate for the impacts of NS currents, as claimed in [17], [18], [19], this is not the general case. When the NS voltage drop is not fully compensated, the inverter output voltage cannot be simply assumed to be balanced. Meanwhile, none of

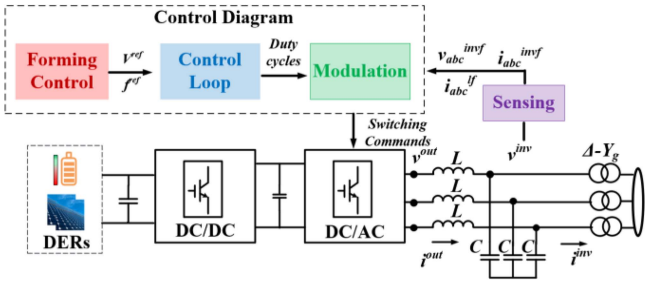


Fig. 1. An IBR with a two-stage interfacing inverter.

the models in [14], [15], [16], [17], [18], [19] considered the potential output virtual impedance or VSG control impacts.

Ref. [20] proposed an impedance model to account for the control loop impacts. However, the model is proposed for transient analyses, and the proposed model is derived under balanced load assumptions.

Moreover, for a three-phase inverter, the NS current will result in second-order (2nd-order) frequency voltage ripples on the dc-link capacitors [21], which may also affect the inverter output voltage. This has also not been considered in the existing literature.

To address the aforementioned issues, in this article, we propose a novel GFM inverter model considering the effects of forming control strategies (voltage droop, virtual impedance, VSG, etc.), control loops, and 2nd-order frequency dc-link voltage ripples. Moreover, we show that the impacts of forming control, control loop, and dc-link voltage ripple on the output voltage are usually not independent from each other. A comprehensive model is proposed to consider these three parts. The proposed model can be used to improve the accuracy of unbalanced power flow analysis with GFM inverters. We show that the proposed model achieves higher accuracy of NS voltage analyses in unbalanced distribution systems compared to the state-of-the-art.

The rest of the article is organized as follows: Section II summarizes the control strategies of GFM inverters; Section III proposes the GFM inverter model and the derivation process; model verification is shown in Section IV; power flow case studies are conducted in Section V to demonstrate the accuracy improvement from the proposed model; Section VI draws the conclusions.

## II. Control Strategies of a GFM Inverter

Three-wire GFM inverters are the most common ones seen in a distribution grid or microgrid formed by IBRs. Three-wire inverters can only provide PS and NS currents. The ZS currents are provided by the step-up transformers with Delta-Yg connections or additional grounding transformers [22]. Therefore, this paper focuses on the modeling of GFM inverters in positive and negative sequences. A typical system diagram of an IBR (Fig. 1) usually contains a two-stage interfacing converter [23]. In this article, we assume the dc-link decouples the dc/dc and dc/ac stages and focus on the modeling of the dc/ac stage.

As shown in Fig. 1, the control of the dc/ac inverter can be divided into three stages. The first stage is the forming control which determines the voltage and frequency characteristics. Examples of forming control include VSG control [24], virtual impedance control [25], droop control [26], etc. The forming control will generate the voltage and frequency references to the second stage, which is the control loop. The control loop will realize the voltage and frequency references to generate duty cycles for the modulation stage. Control loops can be either in stationary coordinates ($\alpha\beta$) [27] or rotatory coordinates ($dq$) [28] and can be single-loop or dual-loop. The third stage is modulation, which transfers the duty cycles to switching commands for the inverter's semiconductor switches. In the present study, we focus on the power flow analysis for fundamental frequency components in the steady state. Therefore, the impacts of the frequency forming control and the modulation stage are trivial, and only the voltage forming control and control loops are considered.

In the following sub-sections, we cover some background knowledge of GFM inverter control. Typical strategies of a GFM inverter are shown in Fig. 2, including the forming control algorithms and control loops.

### A. Forming Control

The forming control contains the algorithms for generating frequency and voltage references. Since the power flow analysis is conducted at the fundamental frequency, the forming control discussion will focus on voltage forming control strategies, including voltage droop control [26], virtual impedance control [25], VSG control with a 2nd-order differential algebraic equation (DAE) model [29], and VSG control with a fourth-order (4th-order) DAE model [30].

*1) Voltage Droop Control:* The voltage droop is usually applied to change the voltage reference based on real-time power feedback. Q-V droop is the most commonly adopted voltage droop control:

$$V_{ref} = V_{ref}^{*} - k_{QV} Q_{inv} \tag{1}$$

where $V_{ref}$ is the voltage reference to the control loop; $V_{ref}^{*}$ is the voltage reference at no load condition; $k_{QV}$is the droop slope; $Q_{inv}$ is the reactive power of the inverter.

*2) Virtual Impedance Control:* The virtual impedance control can be described as:

$$V_{ref} = V_{ref}^{*} - Z_v I_{inv} \tag{2}$$

where $Z_v$ is the added virtual impedance; $I_{inv}$ is the inverter current. When the control reaches the steady state, the PS circuit can be viewed as a controlled voltage source plus an impedance. In the actual implementation, the virtual impedance is usually applied together with the voltage droop control.

*3) VSG With 2nd-Order DAE Electrical Model:* The VSG with a 2nd-order DAE electrical model of a generator can be described as:

$$V_{ref} = E' - (R_a + jX_d') I_{inv} \tag{3}$$

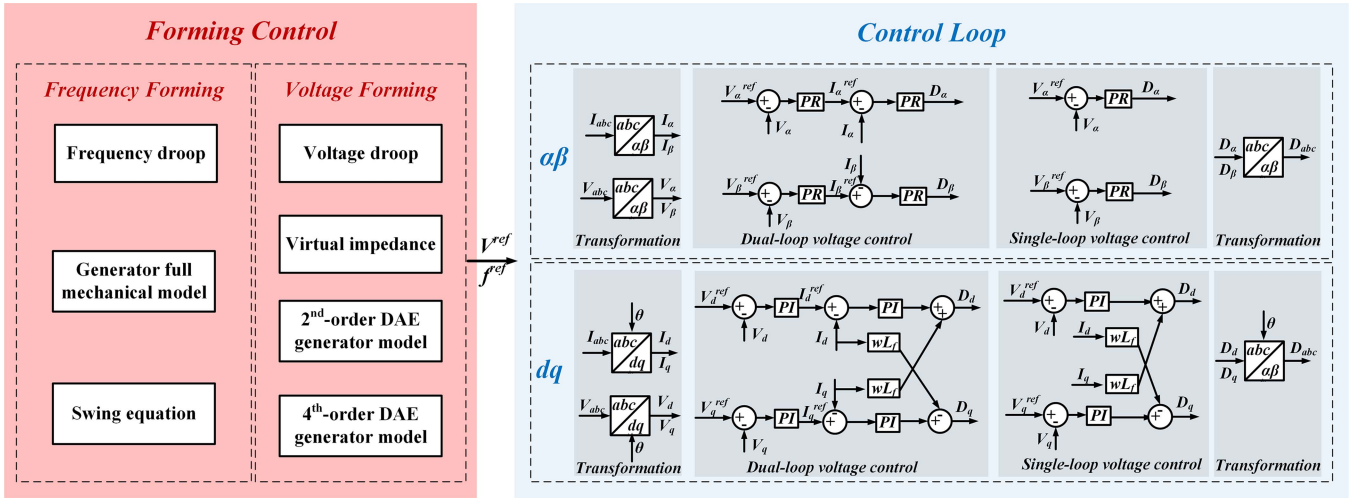


Fig. 2. Forming control strategies and control loops for a GFM inverter.

where $E'$ is the output of the generator excitation model and assumed to be a constant; $R_a$ is the stator resistance and $X'_d$ is the transient reactance of the generator. From the control perspective, the 2nd-order DAE model can be viewed as a virtual impedance with actual generator parameters.

*4) VSG With 4th-Order DAE Electrical Model:* The VSG with a 4th-order DAE electrical model is [30]:

$$V_d^{ref} = E'_d + X'_q I_q - R_a I_d \tag{4a}$$

$$V_q^{ref} = E'_q - X'_d I_d - R_a I_q \tag{4b}$$

$$T'_{q0} \frac{dE'_d}{dt} = -E'_d + (X_q - X'_q) I_q \tag{4c}$$

$$T'_{d0} \frac{dE'_q}{dt} = -E'_q - (X_d - X'_d) I_d + e_{fd} \tag{4d}$$

where $E'_d$ and $E'_q$ are transient back electromotive forces; $X_{d,q}$ and $X'_{d,q}$ are synchronous and transient reactance, respectively; $T'_{q0}$ and $T'_{d0}$ are time constants; $e_{fd}$ is the output of the excitor. The 4th-order DAE model considers the transient performances of a generator and can be utilized for the stability analysis.

## B. Control Loops

Typical control loops for a three-wire GFM inverter can be divided into control loops in $\alpha\beta$ coordinates and control loops in *dq* coordinates. The $\alpha\beta$ transformation is represented as:

$$\boldsymbol{g_{\alpha\beta}} = \frac{2}{3} T_{\alpha\beta} \boldsymbol{g_{abc}} \tag{5}$$

$$\boldsymbol{g_{abc}} = T_{\alpha\beta}^T \boldsymbol{g_{\alpha\beta}} \tag{6}$$

where $T_{\alpha\beta} = \begin{bmatrix} 1 & -\frac{1}{2} & -\frac{1}{2} \\ 0 & \frac{\sqrt{3}}{2} & -\frac{\sqrt{3}}{2} \end{bmatrix}$, $\boldsymbol{g}$ represents the instantaneous voltage ($v$) or current ($i$) vectors. $\alpha\beta$ coordinates are stationary and the three-phase voltages/currents in $\alpha\beta$ coordinates are sinusoidal. Therefore, in $\alpha\beta$ coordinates, proportional-resonant (PR) controllers are usually applied to regulate the voltage and current.

The *dq* transformation is represented as:

$$\boldsymbol{g_{dq}} = \frac{2}{3} T_{dq} \boldsymbol{g_{abc}} \tag{7}$$

$$\boldsymbol{g_{abc}} = T_{dq}^T \boldsymbol{g_{dq}} \tag{8}$$

where $T_{dq} = \begin{bmatrix} \cos\omega t & \cos(\omega t - \frac{2\pi}{3}) & \cos(\omega t + \frac{2\pi}{3}) \\ -\sin\omega t & -\sin(\omega t - \frac{2\pi}{3}) & -\sin(\omega t + \frac{2\pi}{3}) \end{bmatrix}$, *dq* coordinates are rotary. $\omega$ is the rotation speed of coordinates and is generated by the frequency forming control. Proportional-integral (PI) controllers are utilized for the control in *dq* coordinates. Note that, in *dq* coordinates, only the three-phase components that have the same rotation direction as coordinates can be transformed into dc components. A three-phase voltage/current that contains PS and NS components can be written as:

$$\begin{cases} g_a = G_1 \cos(\omega t + \theta_{g1}) + G_2 \cos(\omega t + \theta_{g2}) \\ g_b = G_1 \cos\left(\omega t + \theta_{g1} - \frac{2\pi}{3}\right) + G_2 \cos\left(\omega t + \theta_{g2} + \frac{2\pi}{3}\right) \\ g_c = G_1 \cos\left(\omega t + \theta_{g1} + \frac{2\pi}{3}\right) + G_2 \cos\left(\omega t + \theta_{g2} - \frac{2\pi}{3}\right) \end{cases} \tag{9}$$

where $G_1$ is the PS component, and $G_2$ is the NS component. The voltage/current after $\alpha\beta$ and *dq* transformations are given in (10a) and (10b), respectively.

$$\begin{cases} G_\alpha = G_1 \cos(\omega t + \theta_{g1}) + G_2 \cos(\omega t + \theta_{g2}) \\ G_\beta = G_1 \sin(\omega t + \theta_{g1}) - G_2 \sin(\omega t + \theta_{g2}) \end{cases} \tag{10a}$$

$$\begin{cases} G_d = G_1 \cos\theta_{g1} + G_2 \cos(2\omega t + \theta_{g2}) \\ G_q = G_1 \sin\theta_{g1} - G_2 \sin(2\omega t + \theta_{g2}) \end{cases} \tag{10b}$$

Therefore, when the voltage/current has NS components, after the $\alpha\beta$ transformation, the NS components will be transformed into fundamental frequency components; after the *dq* transformation, the NS components will be transformed into 2nd-order frequency components. The PR controller has infinite gain at fundamental frequency, while the PI controller does not have infinite gain at 2nd-order frequency. As a result, the output

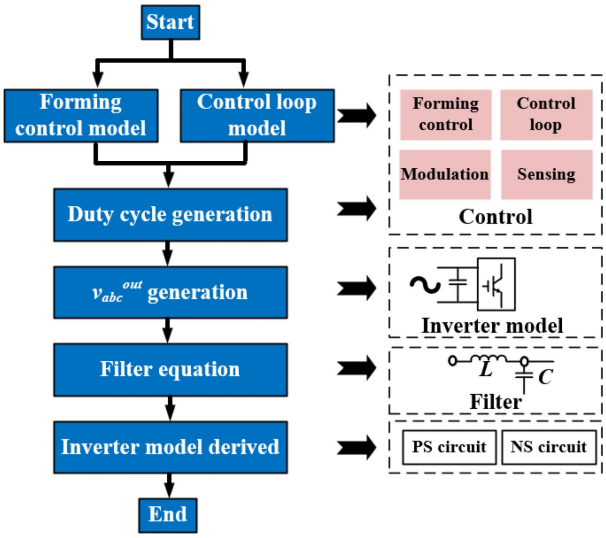


Fig. 3. GFM inverter modeling methodology.

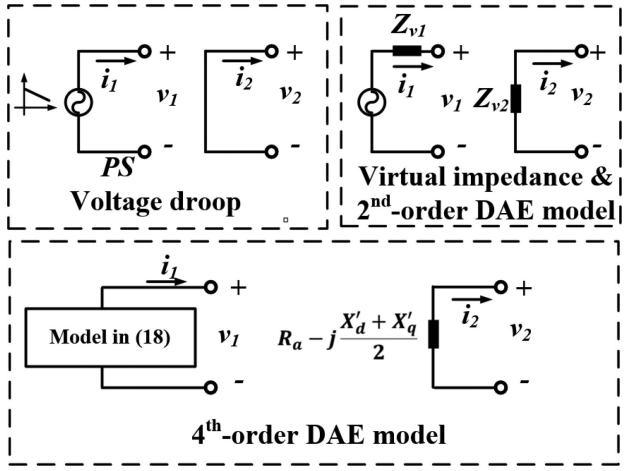


Fig. 4. Modeling of the forming control stage.

voltage can follow the reference without static error in control loops in $\alpha\beta$ coordinates, whereas control loops in *dq* coordinates will have static error. A detailed analysis of the control loop impacts will be provided in the next section.

## III. GFM Inverter Modeling

### A. Modeling Methodology

The modeling methodology is summarized in Fig. 3. The impacts of the forming control and control loops are initially modeled independently for both positive and negative sequences. Then the models of forming control and control loops will be combined to generate the output duty cycles. Based on the duty cycles and inverter model, the inverter output voltage can be calculated. Note that this methodology is for voltage source inverters that are most widely applied. For current source inverters, the output current should be calculated. After the inverter output voltage is derived, an equation can be formulated based on the electrical constraints of the output filter, which can be written as:

$$\begin{cases} \boldsymbol{v}_{\boldsymbol{abc}}^{\boldsymbol{out}} - Z_{lf}\boldsymbol{i}_{\boldsymbol{abc}}^{\boldsymbol{out}} = \boldsymbol{v}_{\boldsymbol{abc}}^{\boldsymbol{inv}} \\ \boldsymbol{i}_{\boldsymbol{abc}}^{\boldsymbol{out}} = \boldsymbol{i}_{\boldsymbol{abc}}^{\boldsymbol{inv}} + Y_{cf}\boldsymbol{v}_{\boldsymbol{abc}}^{\boldsymbol{inv}} \end{cases} \tag{11}$$

where $Z_{lf} \in \mathbb{C}^{3\times3}$ is the impedance matrix of the inverter filter inductor and $Y_{cf} \in \mathbb{C}^{3\times3}$ is the admittance matrix of the filter capacitor; $v_{abc}^{out} \in \mathbb{C}^{3\times1}$ is the three-phase terminal voltage before filters, $v_{abc}^{inv} \in \mathbb{C}^{3\times1}$ is the three-phase voltage that the inverter regulates; $i_{abc}^{out} \in \mathbb{C}^{3\times1}$ is the three-phase current through the filter inductor; $i_{abc}^{inv} \in \mathbb{C}^{3\times1}$ is the three-phase output current of the inverter. Based on (11), the inverter voltage and current relationship can be obtained so that the GFM inverter model can be derived.

### B. Forming Control Modeling

The modeling of the forming control will include models in positive and negative sequences.

*1) Voltage Droop Control:* The voltage droop control, as shown in Fig. 4, is modeled as a controlled-voltage source in the PS circuit. In the NS circuit, it is modeled as a short circuit.

*2) Virtual Impedance and 2nd-Order VSG Control:* For the virtual impedance control and 2nd-order DAE generator model, according to (2) and (3), in the PS circuit, the control can be modeled as a controlled voltage source plus the virtual impedance. In the NS circuit, the control can be modeled as the virtual impedance. According to (10), the PS and NS components in the *q* axis have opposite directions. This may impact the output NS reactance phase angle. For example, in *dq* coordinates, the virtual inductance is realized by adding positive $I_q\omega L_v$ to voltage reference in *d* axis and negative $I_d\omega L_v$ to the reference in *q* axis. However, after inverse *dq* transformation, in NS circuit, this control will result in a virtual capacitance. Therefore, in *dq* coordinates, the virtual impedances can be written as:

$$\begin{cases} Z_{v1} = R_v + jX_v \\ Z_{v2} = R_v - jX_v \end{cases} \tag{12}$$

where $R_v$ and $X_v$ are the virtual impedance in the control loop, $Z_{v1}$ and $Z_{v2}$ are the PS and NS impedances of forming control.

*3) 4th-Order VSG Control:* The 4th-order DAE synchronous generator model is in *dq* coordinates. According to (10), the NS voltage/current will have 2nd-order frequency components. Applying Laplace transformation for (4), in the *s* domain, the model becomes:

$$V_d^{ref} = E'_d(s) + X'_q\left(i_{q1}(s) + i_{q2}(s)\right) - R_a\left(i_{d1}(s) + i_{d2}(s)\right) \tag{13a}$$

$$V_q^{ref} = E'_q(s) - X'_d\left(i_{d1}(s) + i_{d2}(s)\right) - R_a\left(i_{q1}(s) + i_{q2}(s)\right) \tag{13b}$$

$$E'_d(s) = \frac{\left(X_q - X'_q\right)\left(i_{q1}(s) + i_{q2}(s)\right)}{1 + T'_{q0}s} \tag{13c}$$

$$E'_q(s) = -\frac{\left(X_d - X'_d\right)\left(i_{d1}(s) + i_{d2}(s)\right)}{1 + T'_{d0}s} + \frac{e_{fd}(s)}{1 + T'_{d0}s} \tag{13d}$$

where $i_{d1}(s) = \frac{I_1 \cos\theta_{i1}}{s}$ and $i_{q1}(s) = \frac{I_1 \sin\theta_{i1}}{s}$ are s domain PS currents in dq axis;$i_{d2}(s) = I_2 (\frac{\cos\theta_{i2} s}{s^2+4\omega^2} - \frac{2\sin\theta_{i2}\omega}{s^2+4\omega^2})$and $i_{q2}(s) = -I_2 (\frac{2\cos\theta_{i2}\omega}{s^2+4\omega^2} + \frac{\sin\theta_{i2} s}{s^2+4\omega^2})$ are the NS dq currents in the s domain; $e_{fd}(s) = \frac{e_{fd}}{s}$ . When the control reaches the steady state, in the time domain, the PS and NS circuits are different. After taking the inverse Laplace transformation, during the steady state, the PS components will not be changed. The NS currents in the time domain are:

$$i'_{d2}(t) = \mathcal{L}^{-1}\left(\frac{i_{d2}(s)}{1+T'_{d0}s}\right) = \frac{I_2}{\lambda_d}\cos(2\omega t + \theta_{i2} + \psi_{fd}) - \frac{I_2 K_d}{\lambda_d^2} e^{-\frac{t}{T'_{d0}}} \quad (14a)$$

$$i'_{q2}(t) = \mathcal{L}^{-1}\left(\frac{i_{q2}(s)}{1+T'_{q0}s}\right) = \frac{I_2}{\lambda_q}\cos(2\omega t + \theta_{i2} + \psi_{fq}) + \frac{I_2 K_q}{\lambda_q^2} e^{-\frac{t}{T'_{q0}}} \quad (14b)$$

where

$$\begin{cases} \lambda_d = \sqrt{1+4\omega^2 T'^2_{d0}} \\ K_d = \cos\theta_{i2} + 2T'_{d0}\omega\sin\theta_{i2} \\ \psi_{fd} = \arctan -(2T'_{d0}\omega) \end{cases} \quad (15)$$

$$\begin{cases} \lambda_q = \sqrt{1+4\omega^2 T'^2_{q0}} \\ K_d = \sin\theta_{i2} - 2T'_{d0}\omega\cos\theta_{i2} \\ \psi_{fd} = \arctan\frac{1}{2T'_{q0}\omega} \end{cases} \quad (16)$$

Note that the model in (13) is a normalized model. According to $\lambda_d$ and $\lambda_q$ in (15) and (16), since $T'_{d0}$ and $T'_{q0}$ are usually large [31], the 2nd-order frequency components in $E'_d$ and $E'_q$ can be omitted. Therefore, voltage references in the steady state are:

$$\begin{cases} V_d^{ref} = X_q\, i_{q1}(t) - R_a i_{d1}(t) + X'_q i_{q2}(t) - R_a i_{d2}(t) \\ V_q^{ref} = e_{fd}(t) - X_d i_{d1}(t) - R_a i_{q1}(t) - X'_d i_{d2}(t) - R_a i_{q2}(t) \end{cases} \quad (17)$$

where $i_{d1}(t)$ and $i_{q1}(t)$ are dc components; $i_{d2}(t)$ and $i_{q2}(t)$ are 2nd-order frequency components. Separating the PS and NS components in (17), the PS model (18a) is the generic steady-state model of synchronous generators. The NS model (18b) contains transient reactance terms.

$$\begin{cases} V_{d1}^{ref} = X_q i_{q1}(t) - R_a i_{d1}(t) \\ V_{q1}^{ref} = e_{fd}(t) - X_d i_{d1}(t) - R_a i_{q1}(t) \end{cases} \quad (18a)$$

$$\begin{cases} V_{d2}^{ref} = X'_q i_{q2}(t) - R_a i_{d2}(t) \\ V_{q2}^{ref} = -X'_d i_{d2}(t) - R_a i_{q2}(t) \end{cases} \quad (18b)$$

In the NS circuit, after the inverse *dq* transformation, the *dq* coupling terms $X'_q i_{q2}(t)$ and $-X'_d i_{d2}(t)$ in (18b) are:

$$\begin{cases} v_{a2,\,coup}^{ref} = A\sin(3\omega t + \theta_{i2}) - B\sin(\omega t + \theta_{i2}) \\ v_{b2,\,coup}^{ref} = A\sin(3\omega t + \theta_{i2} - \frac{2\pi}{3}) - B\sin(\omega t + \theta_{i2} + \frac{2\pi}{3}) \\ v_{c2,\,coup}^{ref} = A\sin(3\omega t + \theta_{i2} + \frac{2\pi}{3}) - B\sin(\omega t + \theta_{i2} - \frac{2\pi}{3}) \end{cases}$$

$$A = \frac{I_2(X'_d - X'_q)}{2}, B = \frac{I_2(X'_d + X'_q)}{2} \quad (19)$$

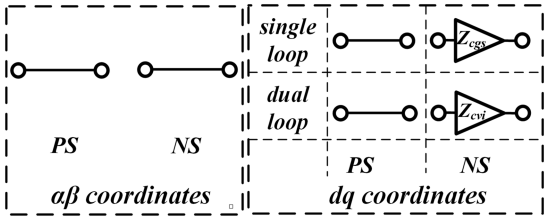


Fig. 5. Modeling of the control loop stage.

The 3rd-order component will not lead to current in a three-wire inverter, meaning that it will not impact the inverter model. After omitting the 3rd-order components, according to (9), (18b), and (19), using phase *a* as an example, the voltage reference is:

$$\begin{cases} v_{a2}^{ref} = \frac{(X'_d + X'_q)}{2} I_2 \cos(\omega t + \theta_{i2} + \frac{\pi}{2}) - R_a i_{a2} \\ i_{a2} = I_2\cos(\omega t + \theta_{i2}) \end{cases} \quad (20)$$

From (20), in the NS circuit, the VSG model is an impedance, and the impedance value is the average of the *dq* transient reactance plus the stator resistance. Note that since the current direction is defined as flowing out of the inverter, the reactance part is capacitive.

### C. Control Loop Modeling

*1) Control Loop in αβ Coordinates:* In $\alpha\beta$ coordinates, both PS and NS components of the voltage/current are at the fundamental frequency. PR controllers are applied to regulate the output voltage/current, therefore, when the control reaches a steady state, the controller can regulate the voltage/current to follow the references with no static error. The control loop will not lead to extra impacts on PS or NS models of the inverter. Thus, it is modeled as a short circuit in Fig. 5.

*2) Control Loop in Dq Coordinates:* In *dq* coordinates, according to (10), the NS components will be transformed into 2nd-order frequency components. Since the PI controller has finite gain at 2nd-order frequency, the control loop will have impacts on the output voltage. For PS components, when the control reaches the steady state, the output voltage/current will follow the reference without static error. The PS circuit can be modeled as a short circuit.

In *dq* coordinates, when the PI controller in the control loop in Fig. 2 is applied to NS components, it can be written as:

$$\begin{cases} G_{out}^d = k_{pg}^d(g_{d2}) + k_{ig}^d \int(g_{d2})\,dt \\ G_{out}^q = k_{pg}^q(g_{q2}) + k_{ig}^q \int(g_{q2})\,dt \end{cases} \quad (21)$$

where *g* can be either voltage or current; $k_{pg}^{d,q}$ and $k_{ig}^{d,q}$ are the PI controller parameters for the voltage/current loop. Note that the parameters of the voltage-loop and current-loop PI controllers in *d* axis are usually the same as the parameters in *q* axis, respectively. We use $k_{pg}$ and $k_{ig}$ to represent those parameters for simplicity. For a single control loop, the input and output

relationships are derived by substituting (10) into (21):

$$\begin{cases} G_{out}^{d} = G_2\ |Z_{cgs}| \cos\left(2\omega t + \theta_{g2} - \psi_{gs}\right) \\ G_{out}^{q} = -G_2 |Z_{cgs}| \sin\left(2\omega t + \theta_{g2} - \psi_{gs}\right) \\ |Z_{cgs}| = \sqrt{\left(k_{pg}\right)^2 + \frac{\left(k_{ig}\right)^2}{4\omega^2}}\ \ \psi_{gs} = \arctan\frac{k_{ig}}{2\omega k_{pg}} \end{cases} \tag{22}$$

Therefore, compared with the NS components in (10), the single PI loop introduces a *complex gain* at 2nd-order frequency:

$$Z_{cgs} = |Z_{cgs}| \angle - \psi_{gs} \tag{23}$$

where *g* can be either voltage (*v*) or current (*i*). For a double loop control (outer voltage loop and inner current loop), after two PI loops, the input and output relationships are:

$$\begin{cases} G_{out}^{d} = G_2\ |Z_{cvi}| \cos\left(2\omega t + \theta_{g2} - \psi_{vi}\right) \\ G_{out}^{q} = -G_2\, |Z_{cvi}| \sin\left(2\omega t + \theta_{g2} - \psi_{vi}\right) \\ |Z_{cvi}| = \sqrt{\left(k_{pv}k_{pi} - \frac{k_{iv}k_{ii}}{4\omega^2}\right)^2 + \left(\frac{k_{iv}k_{pi}}{2\omega} + \frac{k_{pv}k_{ii}}{2\omega}\right)^2} \\ \psi_{vi} = \arctan\frac{\frac{k_{iv}k_{pi}}{2\omega} + \frac{k_{pv}k_{ii}}{2\omega}}{k_{pv}k_{pi} - \frac{k_{iv}k_{ii}}{4\omega^2}} \end{cases} \tag{24}$$

The double-loop control will also introduce *complex gain* at 2nd-order frequency:

$$Z_{cvi} = |Z_{cvi}\ | \angle - \psi_{vi} \tag{25}$$

The control loop models are summarized in Fig. 5.

### D. DC-Link 2nd-Order Frequency Ripple Modeling

In the GFM inverter shown in Fig. 1, NS current on the ac side will result in 2nd-order frequency currents on the dc-link, which can be written as [21]:

$$\tilde{I}_{dc}\ (t) = \frac{3M}{4}\ I_2 \cos\left(2\omega t + \theta_{v1} + \theta_{i2}\right) \tag{26}$$

where *M* is the modulation index; $\theta_{v1}$ and $\theta_{i2}$ are the phase angles for the PS voltage and NS current. The direction of the dc-link current is flowing into the inverter. To protect the DER, the 2nd-order frequency current on the dc-link is blocked by the dc/dc stage. Therefore, the 2nd-order frequency current will go through the dc-link capacitor, resulting in voltage ripples on the dc-link:

$$\begin{aligned} \tilde{V}_{dc}\ (t) &= -\frac{1}{C_{dc}} \int \tilde{I}_{dc}\,(t)\, dt + R_{dc}\tilde{I}_{dc}\,(t) \\ &\approx -\frac{3M}{8\omega C_{dc}} I_2 \sin\left(2\omega t + \theta_{v1} + \theta_{i2}\right) \end{aligned} \tag{27}$$

where $R_{dc}$ is the parasitic resistance of the dc-link capacitor and is usually very small compared to the reactance of the dc-link capacitor. Thus, it can be omitted without much affecting the accuracy. The dc-link ripple will impact the inverter model in Fig. 3. If the dc-link voltage ripple is omitted, the inverter output voltage can be calculated by the generated duty cycles multiplied by one-half of the dc-link voltage. When the dc-link ripple is considered, the inverter output voltage is calculated as:

$$v_{abc}^{out}\ (t) = d_{abc}\ (t)\ \frac{\left(V_{dc} + \tilde{V}_{dc}\,(t)\right)}{2} \tag{28}$$

where the output duty cycles $d_{abc}(t)$ are:

$$\begin{cases} d_a = D_1 \cos\left(\omega t + \theta_{d1}\right) + D_2 \cos\left(\omega t + \theta_{d2}\right) \\ d_b = D_1 \cos\left(\omega t + \theta_{d1} - \frac{2\pi}{3}\right) + D_2 \cos\left(\omega t + \theta_{d2} + \frac{2\pi}{3}\right) \\ d_c = D_1 \cos\left(\omega t + \theta_{d1} + \frac{2\pi}{3}\right) + D_2 \cos\left(\omega t + \theta_{d2} - \frac{2\pi}{3}\right) \end{cases} \tag{29}$$

Multiplying the PS duty cycles by the dc-link voltage ripple:

$$\begin{cases} d_a\,(t) \times \frac{\tilde{V}_{dc}(t)}{2} = k_{dc}\ \left(\cos\left(3\omega t + \theta_{dc3}\right) + \cos\left(\omega t + \theta_{dc}\right)\right) \\ d_b\,(t) \times \frac{\tilde{V}_{dc}(t)}{2} \\ = k_{dc}\left(\cos\left(3\omega t + \theta_{dc3} - \frac{2\pi}{3}\right) + \cos\left(\omega t + \theta_{dc} + \frac{2\pi}{3}\right)\right) \\ d_c\,(t) \times \frac{\tilde{V}_{dc}(t)}{2} \\ = k_{dc}\left(\cos\left(3\omega t + \theta_{dc3} + \frac{2\pi}{3}\right) + \cos\left(\omega t + \theta_{dc} - \frac{2\pi}{3}\right)\right) \end{cases} \tag{30}$$

where $k_{dc} = -\frac{3M}{32\omega C_{dc}} I_2 D_1$, $\theta_{dc} = \theta_{v1} + \theta_{i2} - \theta_{d1} - \frac{\pi}{2}$ and $\theta_{dc3} = \theta_{v1} + \theta_{i2} + \theta_{d1} - \frac{\pi}{2}$. The 3rd-order components will be eliminated by the step-up transformer with Delta-Yg configuration. The fundamental frequency components in (30) become NS, meaning that the PS duty cycles, and 2nd-order frequency dc-link voltage ripples will generate NS components in the output voltage. Similarly, multiplying the NS duty cycles by the dc-link voltage ripple generates 3rd-order and PS fundamental frequency components. However, in the steady state, the NS duty cycles are usually much smaller than PS duty cycles, and the ripple is usually limited by design. Therefore, the 2nd-order frequency ripple impacts on the PS circuit can be neglected and the modeling will focus on the NS circuit.

According to fundamental components in (30), the PS duty cycle ($d_1$) will impact the output NS voltage. In the $\alpha\beta$ coordinates, when the control reaches the steady state, the PR controller can regulate the output voltage to the reference values. Therefore, the dc-link ripple impacts can be compensated by the controller. However, in *dq* coordinates, since the PI controller cannot eliminate 2nd-order frequency components (NS), the dc-link ripple impacts cannot be fully compensated. When sinusoidal pulse width modulation (PWM) is applied, the PS duty cycle magnitude can be approximated by:

$$D_1 \approx \frac{V_1}{\frac{V_{dc}}{2}} = M \tag{31}$$

Examining (9), (26), (30), and (31), the 2nd-order frequency dc voltage ripple will lead to a *complex gain* in the NS circuit:

$$Z_{dc} = -\frac{3M^2}{32\omega C_{dc}} \angle \left(\theta_{v1} - \theta_{d1} - \frac{\pi}{2}\right) \tag{32}$$

### E. GFM Inverter Model Derivation

In $\alpha\beta$ coordinates, the control loop can compensate for the NS voltage to achieve a balanced output voltage. Therefore, the GFM inverter model is the model of its forming control stage, which is summarized in Table I. The equivalent circuits are shown in Fig. 6. The control loop and dc-link ripple impacts will not impact the model.

In *dq* coordinates, since the PI controller has no static error on dc components, the control loop will not impact the PS output voltage. The PS model of a GFM inverter is the model of the forming control. For the NS model, (11) will be used for the

TABLE I
NS MODELS OF GFM INVERTERS

| Forming control (NS Model) | Control Loop | Overall GFM Model |
|---|---|---|
| Voltage droop ($Z_{vfm}=0$) | Single $dq$: $Z_{cvs}=-\lvert Z_{cvs}\rvert\angle-\psi_{vs}$ (V loop gain) | $Z_{inv2}=-\dfrac{k_{i2}Z_{vfm}Z_{cvs}+(1-k_{i2})Z_{Lf}-Z_{dc}}{k_{v2}Z_{cvs}+1-\frac{Z_{dc}}{Z_{cf}}+(1-k_{i2})\frac{Z_{Lf}}{Z_{cf}}}$ |
| Virtual impedance ($Z_{vfm}$ self-defined) | | |
| 2nd-order DAE generator ($Z_{vfm}=R_a-jX_d$) | Dual $dq$: $Z_{cis}=-\lvert Z_{cis}\rvert\angle-\psi_{is}$ (I loop gain) $Z_{cvi}=-\lvert Z_{cvi}\rvert\angle-\psi_{vi}$ (VI loop gain) | $Z_{inv2}=-\dfrac{k_{i2}Z_{vfm}Z_{cvi}+k_{i2}Z_{cis}+(1-k_{i2})Z_{Lf}-Z_{dc}}{k_{v2}Z_{cvi}+1+k_{i2}\frac{Z_{cis}}{Z_{cf}}-\frac{Z_{dc}}{Z_{cf}}+(1-k_{i2})\frac{Z_{Lf}}{Z_{cf}}}$ |
| 4th-order DAE generator ($Z_{vfm}=R_a-j\frac{X'_d+X'_q}{2}$) | | |
| Voltage droop ($Z_{vfm}=0$) | Single/dual loop control using PR controller in $\alpha\beta$ coordinates: short circuit | Single/dual loop: $Z_{inv2}=Z_{vfm}$ |
| Virtual impedance ($Z_{vfm}$ self-defined) | | |
| 2nd-order DAE generator ($Z_{vfm}=R_a-jX_d$) | | |
| 4th-order DAE generator ($Z_{vfm}=R_a-j\frac{X'_d+X'_q}{2}$) | | |

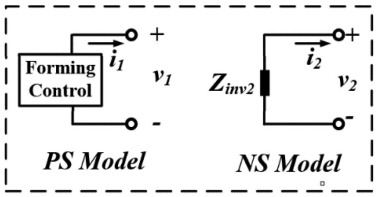


Fig. 6. GFM inverter model.

model derivation. According to Fig. 1, the output voltage will be sampled back to the converter; the sampling usually scales down the measurement value and filters out switching frequency harmonics. To avoid the potential impacts on the control, the cut-off frequency of the low-pass filter is usually much higher than the fundamental frequency. Therefore, the sampling stage can be modeled by a scaling factor.

In the NS circuit, based on the aforementioned discussion, the forming control stage can be modeled as impedances (for the voltage droop case, the impedance value can be viewed as zero). To simplify the derivation, $Z_{vfm}=R_{fm}-X_{fm}$ is used to represent the NS impedance of the forming control. For a single voltage loop control shown in Fig. 2, considering the forming control stage, the inverter output duty cycles can be written as:

$$\begin{cases} d_{d2}=PI_v^d\left(k_{if}\left(-R_{fm}i_{d2}+X_{fm}i_{q2}-k_{vf}v_{d2}\right)\right) \\ \qquad\qquad +k_{if}\omega L_f i_{q2} \\ d_{q2}=PI_v^q\left(k_{if}\left(-R_{fm}i_{q2}-X_{fm}i_{d2}-k_{vf}v_{q2}\right)\right) \\ \qquad\qquad -k_{if}\omega L_f i_{d2} \end{cases} \tag{33}$$

where $k_{if}$ and $k_{vf}$ are scaling ratios of the sampling stage. After inverse $dq$ transformation in (8) and considering dc-link voltage ripple impacts in (30), using phasor representation, the output NS voltage can be represented as:

$$\begin{aligned} \vec{V}_2^{out}=&-k_{i2}\,Z_{vfm}Z_{cvs}\vec{I}_2^{inv}+k_{i2}Z_{lf}\vec{I}_2^{out} \\ &+Z_{dc}\vec{I}_2^{out}-k_{v2}Z_{cvs}\vec{V}_2^{inv} \end{aligned} \tag{34}$$

where $\vec{V}_2^{out}$ and $\vec{V}_2^{inv}$ are the inverter NS output voltage and terminal voltage; $\vec{I}_2^{out}$ and $\vec{I}_2^{inv}$ are the inverter NS output current and NS current flowing out of the terminals; $k_{i2}=\frac{k_{if}V_{dc}}{2}$, $k_{v2}=\frac{k_{vf}V_{dc}}{2}$. According to (11) and (34), the relationship between the NS terminal voltage and NS terminal current can be represented as:

$$\vec{V}_2^{inv}=Z_{inv2}\,\vec{I}_2^{inv} \tag{35}$$

where

$$Z_{inv2}=-\frac{k_{i2}Z_{vfm}Z_{cvs}+(1-k_{i2})\,Z_{Lf}-Z_{dc}}{k_{v2}Z_{cvs}+1-\frac{Z_{dc}}{Z_{cf}}+(1-k_{i2})\,\frac{Z_{Lf}}{Z_{cf}}} \tag{36}$$

For the dual-loop control, a similar relationship can be obtained, the impedance is written as:

$$Z_{inv2}=-\frac{k_{i2}Z_{vfm}Z_{cvi}+k_{i2}Z_{cis}+(1-k_{i2})\,Z_{Lf}-Z_{dc}}{k_{v2}Z_{cvi}+1+k_{i2}\frac{Z_{cis}}{Z_{cf}}-\frac{Z_{dc}}{Z_{cf}}+(1-k_{i2})\,\frac{Z_{Lf}}{Z_{cf}}} \tag{37}$$

$Z_{inv2}$ can be considered as an impedance in the NS circuit. The NS impedance model considers the impacts of the forming control, control loop, and the 2nd-order frequency dc-link voltage ripple. For control in both $dq$ and $\alpha\beta$ coordinates, the PS model will follow the forming control model. The NS model will behave as an impedance. A generalized GFM inverter model is summarized in Fig. 6 and the NS impedances are summarized in Table I.

Since most unbalanced power flow analyses are conducted using algorithms for three-phase systems, the GFM inverter model can be converted to a voltage source followed by a three-phase impedance. The impedance matrix is given by:

$$\begin{aligned} Z_{eq}&=AZ_{inv}A^{-1} \\ Z_{inv}&=\begin{bmatrix}0&0&0\\0&Z_{inv1}&0\\0&0&Z_{inv2}\end{bmatrix} \\ A&=\begin{bmatrix}1&1&1\\1&a^2&a\\1&a&a^2\end{bmatrix},\ a=e^{j\frac{2\pi}{3}} \end{aligned} \tag{38}$$

Note that $Z_{eq}$ is not full rank since the GFM inverter is three-wire. In practice, $Z_{eq}$ can be combined with the impedance matrix of the step-up transformer to make the system bus admittance matrix invertible.

## IV. MODEL VERIFICATION

The derived model is verified in MATLAB Simulink with the circuit shown in Fig. 7. The detailed parameters are summarized in Table II. A two-level voltage source inverter is modeled using

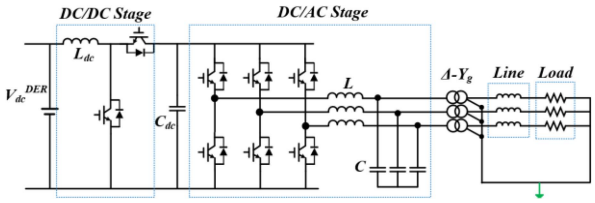


Fig. 7. Circuit of the derived model verification.

TABLE II
PARAMETERS OF THE MODEL VERIFICATION CIRCUIT

| Parameter | | Values |
|---|---|---|
| System setup | | $V_{ac} = 480\ V, S_{base} = 4\ MW$<br>$V_{dc} = 1020\ V, V_{dc}^{DER} = 425\ V$<br>$P_{load}^{a} = 1.333\ MW, P_{load}^{b} = P_{load}^{c} = 1\ kW$ |
| Converter parameters | | $L = 6.11\ \mu H\ (R_L = 1.44\ \mu\Omega)$<br>$C = 4.6\ mF (R_c = 0.0125\Omega)$<br>$L_{dc} = 18\ \mu H, C_{dc} = 12.7\ mF\ (R_{dc} = 0.01\Omega)$ |
| Control parameters | $dq$ | $k_{pv} = 0.0625, k_{iv} = 312.5$ (Single loop)<br>$k_{pv} = 0.25, k_{iv} = 1250, k_{pi} = 0.48, k_{ii} = 52.2$ |
| | $\alpha\beta$ | $k_{prv} = 0.333, k_{rv} = 2000$ (Single loop)<br>$k_{prv} = 0.1, k_{rv} = 100, k_{pri} = 0.02, k_{ri} = 20$<br>$\omega_{cv} = \omega_{ci} = 2\ rad/s$ |
| | | $f_s = 10\ kHz, k_{if} = 1.47 \times 10^{-4}, k_{vf} = 0.0026$ |
| Generator model | | $X_d = 3.4375\ (pu), X_q = 1.7499(pu), R_a = 0.0023(pu)$<br>$X'_d = 0.2626\ (pu), X'_q = 0.3026(pu)$<br>$X''_d = 0.1836\ (pu), X''_q = 0.1790\ (pu)$<br>$T'_{d0} = 2.389\ s, T'_{q0} = 0.3982\ s$<br>$T''_{d0} = 0.0091\ s, T''_{q0} = 0.0069\ s$ |
| Virtual impedance | | $R_v = 0.03\ (pu), X_v = 0.15(pu)$ |
| Droop slope | | $k_{QV} = 0.05$ |

the switching model and includes the dc/ac stage and a boost converter as the dc/dc stage. 2nd-order frequency current control is implemented in the dc/dc stage to avoid dc current flowing into the DER [32]. Note that if the dc 2nd-order frequency current is fully provided by the DER and dc/dc stage, the dc ripple impacts ($Z_{dc}$) will become zero.

Different forming control algorithms and loops are simulated. All control algorithms are realized in the model in Fig. 7. The PS and NS impedances are calculated using measurements in the model. They are assumed to be the ground truth for comparison with the derived models. Since the 4th-order DAE generator model is realized in $dq$ coordinates, to achieve the 4th-order DAE generator model with control loops in $\alpha\beta$ coordinates, the generated voltage references are transformed from $dq$ coordinates to $\alpha\beta$ coordinates.

From the derived model, the NS performances of all the aforementioned algorithms are impedances. Therefore, the NS impedance can be directly measured by the inverter output NS voltage and current. For the PS impedance, since the 4th-order DAE generator model is in $dq$ coordinates, the PS output can be viewed as a voltage source and a fixed impedance. Therefore, the verification of the 4th-order DAE generator model focuses on the NS model. The PS impedance of other models are measured by the voltage difference over the current difference. The voltage difference ($\Delta\vec{V}_1$) and current difference ($\Delta\vec{I}_1$) are gathered by introducing load steps in the simulation. Note that the direction of the measured current is flowing out of the inverter.

The verification results are summarized in Table III, where the calculated PS/NS impedance and measured PS/NS impedance are compared. The output voltage and inductor current waveforms are summarized in Fig. 8, where with different control algorithms, the output voltage unbalance is different under the same load condition. This shows that different control algorithms have different impacts on the NS model of the GFM inverter. The voltage unbalance factor $V_{unb}$, defined as the NS voltage divided by the PS voltage [1], is proportional to the NS impedance of the GFM inverter, since the load current remains the same for all cases. For example, as shown in Table III, the dual loop control in $dq$ coordinates has the largest impedance. This corresponds to Fig. 8(d), where the voltage unbalance factor is 12.13%.

In $\alpha\beta$ coordinates, the measured PS and NS impedances match the derived results with neglectable errors. This is because the PR controller used in $\alpha\beta$ coordinates can regulate the output voltage to the reference value, so the dc-link ripple has no impact on the equivalent impedances.

In $dq$ coordinates, the measured PS impedances match the derived results, while the NS impedances have some error. For dual-loop controls, the error of the NS voltage amplitude is less than 5% and the phase error is less than 2%. For the single-loop controls, the error of the NS voltage amplitude is less than 15% and the phase error is less than 20%. However, the derived NS impedances are also more accurate than the models in [14], [15], [16] and [17], [18], [19], which are summarized in Table IV. The gaps between the derived values and measured values come from the inverter switching actions and the NS impedance introduced by the dc-link ripple. For dc-ripple impacts, the derivation of (26) in [21] assumes that the output voltage only contains PS and ZS components. However, the output voltages of inverters may also contain NS components that can affect the dc current ripples. The contribution of NS voltage on the dc link current ripples is very small as compared to the PS voltage and is hence omitted in this study. Meanwhile, PS duty cycle amplitude is assumed to be the modulation index in (31), which also introduces minimal modeling error. In addition to control loops, the output NS impedance will also be impacted by the non-ideal part of the inverter such as the on-resistance of semiconductor devices.

From the impedance value perspective, the forming control is usually designed to introduce inductive impedances. Therefore, the NS impedances introduced by the forming control are capacitive, which can cause potential resonance with other sources that have inductive NS impedances such as synchronous generators [31]. The $dq$ control loops will introduce inductive impedances, therefore, the $dq$ control loop can partially compensate for the NS impedances generated by the forming control. Taking dual-loop control as an example, the forming control impedance of the 4th-order DAE generator model is higher than the virtual impedance control, however, the eventual output NS impedance amplitude of the 4th-order DAE generator model control is smaller than the virtual impedance control.

TABLE III
MODEL VERIFICATION SUMMARY

| Control loop | Forming control | Calculated PS impedance | Measured PS impedance | Calculated NS impedance | Measured NS impedance |
|---|---|---|---|---|---|
| Single loop in *dq* coordinates | Voltage droop | 0 | $\lvert\vec{Z}_{vc1}\rvert < 5\times10^{-4}$ | $0.0095\angle103.5^{\circ}$ | $0.0085\angle131.0^{\circ}$ |
| | Virtual impedance | $0.0088\angle-101.3^{\circ}$ | $0.0088\angle-103.2^{\circ}$ | $0.0094\angle97.4^{\circ}$ | $0.0084\angle105.0^{\circ}$ |
| | 4th-order generator | Not available | Not available | $0.0098\angle91.2^{\circ}$ | $0.0091\angle80.5^{\circ}$ |
| Dual loop in *dq* coordinates | Voltage droop | 0 | $\lvert\vec{Z}_{vc1}\rvert < 5\times10^{-4}$ | $0.0297\angle-149.7^{\circ}$ | $0.0306\angle-147.8^{\circ}$ |
| | Virtual impedance | $0.0088\angle-101.3^{\circ}$ | $0.0088\angle-103.9^{\circ}$ | $0.0237\angle-157.3^{\circ}$ | $0.0243\angle-155.6^{\circ}$ |
| | 4th-order generator | Not available | Not available | $0.0178\angle-162.8^{\circ}$ | $0.0181\angle-158.0^{\circ}$ |
| Single loop in *αβ* coordinates | Voltage droop | 0 | $\lvert\vec{Z}_{vc1}\rvert < 5\times10^{-4}$ | 0 | $\lvert\vec{Z}_{vc2}\rvert < 5\times10^{-4}$ |
| | Virtual impedance | $0.0088\angle-101.3^{\circ}$ | $0.0089\angle103.2^{\circ}$ | $0.0088\angle101.3^{\circ}$ | $0.0089\angle100.5^{\circ}$ |
| | 4th-order generator | Not available | Not available | $0.0162\angle89.5^{\circ}$ | $0.0163\angle88.4^{\circ}$ |
| Dual loop in *αβ* coordinates | Voltage droop | 0 | $\lvert\vec{Z}_{vc1}\rvert < 5\times10^{-4}$ | 0 | $\lvert\vec{Z}_{vc2}\rvert < 5\times10^{-4}$ |
| | Virtual impedance | $0.0088\angle-101.3^{\circ}$ | $0.0090\angle-104.3^{\circ}$ | $0.0088\angle101.3^{\circ}$ | $0.0089\angle103.5^{\circ}$ |
| | 4th-order generator | Not available | Not available | $0.0162\angle89.5^{\circ}$ | $0.0163\angle89.3^{\circ}$ |

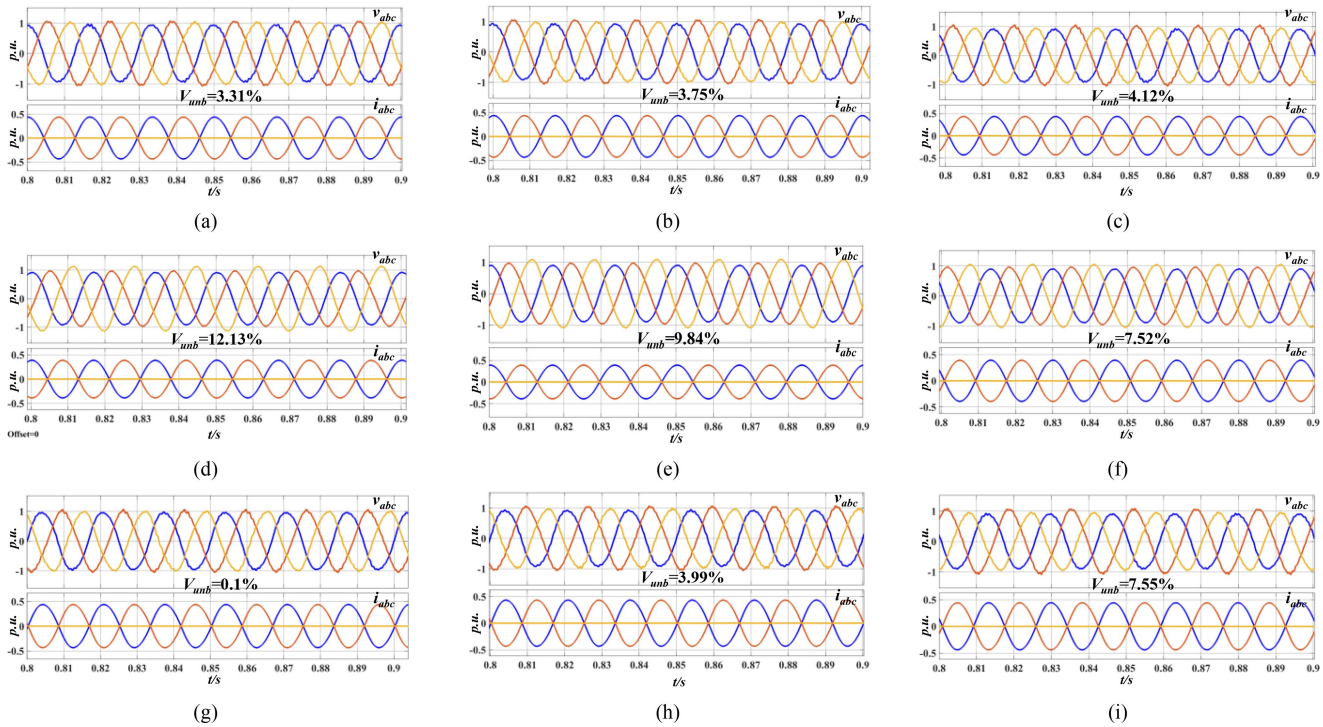


Fig. 8. Simulation waveforms of different control algorithms: (a) voltage droop with single loop (*dq*); (b) virtual impedance with single loop (*dq*); (c) 4th-order generator with single loop (*dq*); (d) voltage droop with dual loop (*dq*); (e) virtual impedance with dual loop (*dq*); (f) 4th-order generator with dual loop (*dq*); (g) voltage droop (*αβ*); (h) virtual impedance with single loop (*αβ*); (i) 4th-order generator with single loop (*αβ*).

TABLE IV
IMPEDANCE IN EXISTING LITERATURES

| | PS impedance* | NS impedance* |
|---|---|---|
| Ref. [14-16] (filter impedance) | 0 | $0.0023\angle-91.4^{\circ}$ |
| Ref. [17-19] (short circuit) | 0 | 0 |
| Ref. [13] (virtual impedance) | $0.0088\angle-101.3^{\circ}$ | $0.0088\angle-101.3^{\circ}$ |
| *Current direction for impedance calculation is flowing out of the inverter | | |

## V. POWER FLOW ANALYSIS RESULTS

In this section, we investigate the impacts of the proposed GFM inverter model on the power flow analysis. The proposed model is compared with the inverter models in the existing literature [13], [14], [15], [16], [17], [18], [19], which can be classified into three models: *filter impedance model* [14], [15], [16], *short-circuit model* [17], [18], [19], and *virtual impedance model* [13].

The inverter (parameters given in Table II) replaces the substation buses in IEEE 13-bus and 34-bus systems to serve as the source. In the case study, the IEEE 13 and 34 bus system models are built in MATLAB Simulink (time step is 2e-6 s). Time domain simulations are conducted, and bus voltages are measured. The measured voltages are used as the baseline for the comparison with the power flow analysis.

The power flow is calculated in OpenDSS [33], where the proposed model and models in the existing literature are compared. The PS and NS impedances are modeled as reactors and connected to the sources. In the Simulink model, loads are

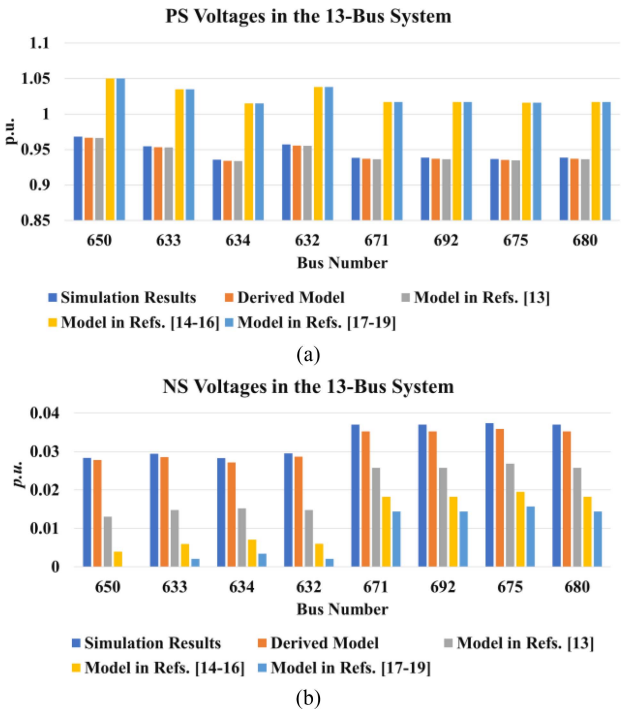


Fig. 9. Testing results in the 13-bus system.

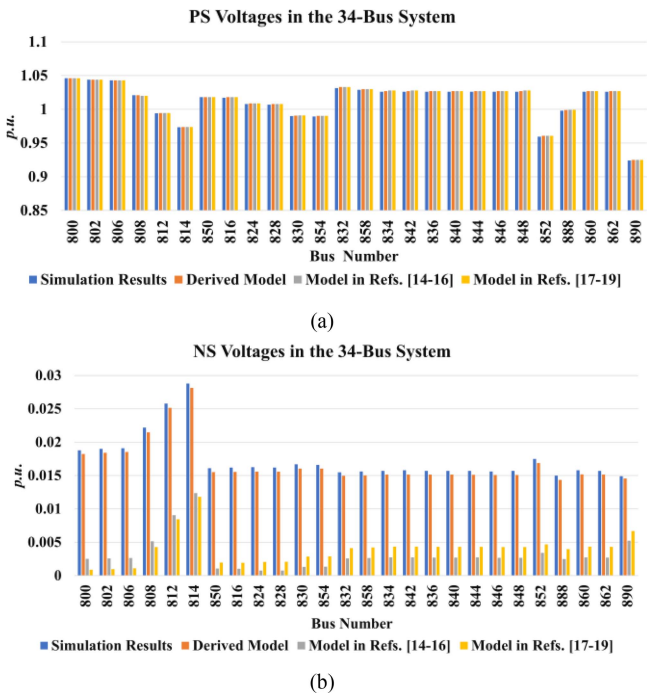


Fig. 10. Testing results in the 34-bus system.

realized by "Three-phase Series RLC Load", which are constant impedance loads in time domain simulation. Therefore, all the load models in OpenDSS are changed to constant impedance loads. Note that since during the derivation, the NS current direction is out of the inverter, the actual NS impedance applied in the model should have a 180-degree phase shift.

### A. 13-Bus System

In this case, a dual-loop voltage control loop with virtual impedance forming control is applied to the inverter. After a 180-degree phase shift, the inverter PS and NS impedances are $0.0088\angle 78.7°\Omega$ and $0.0237\angle 22.7°\Omega$, respectively. The power flow analysis results of the 13-bus system are shown in Fig. 9, where the PS and NS voltages of different buses are listed. Since PS and NS voltages are defined for three-phase buses, PS and NS voltages of non-three-phase buses are not listed. According to Fig. 9, for PS voltages, the results from the derived model and the virtual impedance model [13] match the baseline simulation ones, while the results from the filter impedance models [14], [15], [16] and short circuit models [17], [18], [19] have more than 30% error. For the NS voltage, the derived model and the models in the existing literature have significantly different results. Based on the baseline simulation results, the derived model has less than 5% error while the virtual impedance model has more than 30% error and the filter impedance models [14], [15], [16] and short circuit models [17], [18], [19] have more than 50% error. This indicates that the derived model accurately captured the impacts of the GFM inverter control using an equivalent impedance in NS, and it achieved significant accuracy improvement in the calculated NS voltage without losing the accuracy of PS voltages.

### B. 34-Bus System

In this case, the voltage droop control with dual-loop control in *dq* coordinates is applied to the GFM inverter. The short circuit and filter impedance models are also applied for comparison. Note that since the forming control is droop, the virtual impedance model is the same as the short circuit model. The PS impedance is zero and the NS impedance is $0.0297\angle 30.3°\Omega$ after a 180-degree phase shift. The results of the 34-bus system are shown in Fig. 10, where the calculated PS voltages of all the models are accurate (less than 2% error). For the NS voltages, the derived model still shows less than 5% prediction error while the existing models have more than 50% error.

The proposed GFM inverter power flow model achieves significant improvement in NS voltage accuracy over the state-of-the-art methods. This shows that the various control algorithms implemented in GFM inverters have significant impacts on the accuracy of the equivalent power flow model, especially under unbalanced conditions. Adding the equivalent NS impedance in the GFM inverter power flow model is necessary to accurately reflect the output of the GFM inverter in unbalanced conditions.

## VI. Conclusion

Existing GFM inverter models have not fully considered the impacts of its control, especially under unbalanced conditions. In this article, the control effects of grid-forming inverters are modeled, considering different forming control algorithms, control loops, and dc-link voltage ripples.

The PS models of GFM inverters are determined by the forming control, while the NS models are more complex. For the droop control, the NS forming control model is a short circuit model. For the virtual impedance control, the virtual inductance in PS is equivalent to a virtual capacitance in NS. For the 4th-order VSG control, the NS forming control model is an impedance, its value being the stator resistance plus a virtual capacitance.

Control loops in $\alpha\beta$ coordinates will not introduce additional elements in the GFM model. Control loops in *dq* coordinates will lead to additional impedances in NS. This control effect is largely neglected in the existing literature.

Considering the impacts of dc-link voltage ripples, the PR controllers used in control loops in $\alpha\beta$ coordinates can compensate for the dc-ripple impacts. However, in *dq* coordinates, the PI controllers do not have infinite gain at 2nd-order frequency, and the dc-ripple will result in an additional impedance in the NS circuit.

In summary, in $\alpha\beta$ coordinates, the GFM inverter model only contains the forming control model; in *dq* coordinates, the GFM inverter model needs to consider the combined impacts of forming control, control loop, and dc-link voltage ripples.

The derived models are applied in power flow analyses in the IEEE 13-bus and 34-bus systems and compared with the GFM models in the existing literature. The results show that by using the derived model, the power flow analysis can achieve high calculation accuracy for both the PS and NS voltages. Using time-domain simulation results as baselines, the error of NS voltage calculated using the proposed model is less than 5% compared to more than 30% using the existing models. In addition, the derived model can be easily integrated into existing power flow models by modifying the impedance matrix, and will not introduce penalties in terms of computational effort.

## ACKNOWLEDGMENT

The views expressed herein do not necessarily represent the views of the U.S. Department of Energy or the United States Government. The United States Government retains and the publisher, by accepting the article for publication, acknowledges that the United States Government retains a non-exclusive, paid-up, irrevocable, world-wide license to publish or reproduce the published form of this manuscript, or allow others to do so, for United States Government purposes. The Department of Energy will provide public access to these results of federally sponsored research in accordance with the DOE Public Access Plan (http://energy.gov/downloads/doe-public-access-plan).

## REFERENCES

[1] *IEEE Recommended Practice for Electric Power Distribution for Industrial Plants*, IEEE Standard 141-1993, Apr. 1994.

[2] A. Pandey, M. Jereminov, M. R. Wagner, D. M. Bromberg, G. Hug, and L. Pileggi, "Robust power flow and three-phase power flow analyses," *IEEE Trans. Power Syst.*, vol. 34, no. 1, pp. 616–626, Jan. 2019.

[3] M. B. Delghavi and A. Yazdani, "Sliding-mode control of AC voltages and currents of dispatchable distributed energy resources in master-slave-organized inverter-based microgrids," *IEEE Trans. Smart Grid*, vol. 10, no. 1, pp. 980–991, Jan. 2019.

[4] J. D. Watson, Y. Ojo, K. Laib, and I. Lestas, "A scalable control design for grid-forming inverters in microgrids," *IEEE Trans. Smart Grid*, vol. 12, no. 6, pp. 4726–4739, Nov. 2021.

[5] M. M. A. Abdelaziz, H. E. Farag, E. F. El-Saadany, and Y. A. -R. I. Mohamed, "A novel and generalized three-phase power flow algorithm for islanded microgrids using a newton trust region method," *IEEE Trans. Smart Grid*, vol. 28, no. 1, pp. 190–201, Feb. 2013.

[6] A. A. Eajal, M. A. Abdelwahed, E. F. El-Saadany, and K. Ponnambalam, "A unified approach to the power flow analysis of AC/DC hybrid microgrids," *IEEE Trans. Sustain. Energy*, vol. 7, no. 3, pp. 1145–1158, Jul. 2016.

[7] L. Ren and P. Zhang, "Generalized microgrid power flow," *IEEE Trans. Smart Grid*, vol. 9, no. 4, pp. 3911–3913, Jul. 2018.

[8] H. Wang, Z. Yan, X. Xu, and K. He, "Evaluating influence of variable renewable energy generation on islanded microgrid power flow," *IEEE Access*, vol. 6, pp. 71339–71349, 2018.

[9] G. Agundis-Tinajero et al., "Extended-optimal-power-flow-based hierarchical control for islanded AC microgrids," *IEEE Trans. Power Electron.*, vol. 34, no. 1, pp. 840–848, Jan. 2019.

[10] Z. Wang, F. Liu, Y. Chen, S. H. Low, and S. Mei, "Unified distributed control of stand-alone DC microgrids," *IEEE Trans. Smart Grid*, vol. 10, no. 1, pp. 1013–1024, Jan. 2019.

[11] V. C. Cunha, T. Kim, P. Siratarnsophon, N. Barry, S. Santoso, and W. Freitas, "Quasi-static time-series power flow solution for islanded and unbalanced three-phase microgrids," *IEEE Open Access J. Power Energy*, vol. 8, pp. 97–106, 2021.

[12] Y. Liu, Z. Li, and M. Fan, "A Newton–Raphson-based sequential power flow algorithm for hybrid AC/DC microgrids," *IEEE Trans. Ind. Appl.*, vol. 58, no. 1, pp. 843–854, Jan./Feb. 2022.

[13] C. Li, S. K. Chaudhary, M. Savaghebi, J. C. Vasquez, and J. M. Guerrero, "Power flow analysis for low-voltage AC and DC microgrids considering droop control and virtual impedance," *IEEE Trans. Smart Grid*, vol. 8, no. 6, pp. 2754–2764, Nov. 2017.

[14] M. Z. Kamh and R. Iravani, "Unbalanced model and power-flow analysis of microgrids and active distribution systems," *IEEE Trans. Power Del.*, vol. 25, no. 4, pp. 2851–2858, Oct. 2010.

[15] M. Z. Kamh and R. Iravani, "A unified three-phase power-flow analysis model for electronically coupled distributed energy resources," *IEEE Trans. Power Del.*, vol. 26, no. 2, pp. 899–909, Apr. 2011.

[16] Y. Ju, W. Liu, Z. Zhang, and R. Zhang, "Distributed three-phase power flow for AC/DC hybrid networked microgrids considering converter limiting constraints," *IEEE Trans. Smart Grid*, vol. 13, no. 3, pp. 1691–1708, May 2022.

[17] M. A. Allam, A. A. Hamad, and M. Kazerani, "A generic modeling and power-flow analysis approach for isochronous and droop-controlled microgrids," *IEEE Trans. Power Syst.*, vol. 33, no. 5, pp. 5657–5670, Sep. 2018.

[18] M. A. Allam, A. A. Hamad, and M. Kazerani, "A sequence-component-based power-flow analysis for unbalanced droop-controlled hybrid AC/DC microgrids," *IEEE Trans. Sustain. Energy*, vol. 10, no. 3, pp. 1248–1261, Jul. 2019.

[19] E. E. Pompodakis, G. C. Kryonidis, C. Demoulias, and M. C. Alexiadis, "A generic power flow algorithm for unbalanced islanded hybrid AC/DC microgrids," *IEEE Trans. Power Syst.*, vol. 36, no. 2, pp. 1107–1120, Mar. 2021.

[20] Y. Li, Y. Gu, Y. Zhu, A. Junyent-Ferré, X. Xiang, and T. C. Green, "Impedance circuit model of grid-forming inverter: Visualizing control algorithms as circuit elements," *IEEE Trans. Power Electron.*, vol. 36, no. 3, pp. 3377–3395, Mar. 2021.

[21] X. Pei, W. Zhou, and Y. Kang, "Analysis and calculation of DC-link current and voltage ripples for three-phase inverter with unbalanced load," *IEEE Trans. Power Electron.*, vol. 30, no. 10, pp. 5401–5412, Oct. 2015.

[22] L. Zhu et al., "A smart and flexible microgrid with a low-cost scalable open-source controller," *IEEE Access*, vol. 9, pp. 162214–162230, 2021.

[23] B. Pawar, E. I. Batzelis, S. Chakrabarti, and B. C. Pal, "Grid-forming control for solar PV systems with power reserves," *IEEE Trans. Sustain. Energy*, vol. 12, no. 4, pp. 1947–1959, Oct. 2021.

[24] A. Fathi, Q. Shafiee, and H. Bevrani, "Robust frequency control of microgrids using an extended virtual synchronous generator," *IEEE Trans. Power Syst.*, vol. 33, no. 6, pp. 6289–6297, Nov. 2018.

[25] B. Fan et al., "A novel droop control strategy of reactive power sharing based on adaptive virtual impedance in microgrids," *IEEE Trans. Ind. Electron.*, vol. 69, no. 11, pp. 11335–11347, Nov. 2022.

[26] K. De Brabandere, B. Bolsens, J. Van den Keybus, A. Woyte, J. Driesen, and R. Belmans, "A voltage and frequency droop control method for parallel inverters," *IEEE Trans. Power Electron.*, vol. 22, no. 4, pp. 1107–1115, Jul. 2007.
[27] S. Yazdani, M. Ferdowsi, M. Davari, and P. Shamsi, "Advanced current-limiting and power-sharing control in a PV-based grid-forming inverter under unbalanced grid conditions," *IEEE J. Emerg. Sel. Topics Power Electron.*, vol. 8, no. 2, pp. 1084–1096, Jun. 2020.
[28] X. Quan et al., "Photovoltaic synchronous generator: Architecture and control strategy for a grid-forming PV energy system," *IEEE J. Emerg. Sel. Topics Power Electron.*, vol. 8, no. 2, pp. 936–948, Jun. 2020.
[29] M. Ren, T. Li, K. Shi, P. Xu, and Y. Sun, "Coordinated control strategy of virtual synchronous generator based on adaptive moment of inertia and virtual impedance," *IEEE J. Emerg. Sel. Topics Circuits Syst.*, vol. 11, no. 1, pp. 99–110, Mar. 2021.
[30] Y. Ma, W. Cao, L. Yang, F. Wang, and L. M. Tolbert, "Virtual synchronous generator control of full converter wind turbines with short-term energy storage," *IEEE Trans. Ind. Electron.*, vol. 64, no. 11, pp. 8821–8831, Nov. 2017.
[31] P. Kundur, *Power System Stability and Control*. New York, NY, USA: McGraw-Hill, 1994, pp. 872–903.
[32] G. Zhu, X. Ruan, L. Zhang, and X. Wang, "On the reduction of second harmonic current and improvement of dynamic response for two-stage single-phase inverter," *IEEE Trans. Power Electron.*, vol. 30, no. 2, pp. 1028–1041, Feb. 2015.
[33] R. C. Dugan and T. E. McDermott, "An open source platform for collaborating on smart grid research," in *Proc. IEEE Power Energy Soc. Gen. Meeting*, Detroit, MI, USA, 2011, pp. 1–7, doi: 10.1109/PES.2011.6039829.

**Dingrui Li** (Graduate Student Member, IEEE) received the B.S. degree in electrical engineering from Tsinghua University, Beijing, China, in 2017. He is currently working toward the Ph.D. degree with the University of Tennessee, Knoxville, TN, USA. His research interests include control of power converters, medium voltage converters, power converters in grid applications, multi-level converters, and microgrid control.

**Yu Su** (Student Member, IEEE) received the B.S. degree in electrical engineering from Tsinghua University, Beijing, China, in 2015, and the M.S. degree in electrical engineering in 2018 from the University of Tennessee, Knoxville, TN, USA, where he is currently working toward the Ph.D. degree in electrical engineering. His research interests include microgrid design and control optimization, renewable integration in electrical power systems, and applications of machine learning methods in power systems.

**Fred Wang** (Fellow, IEEE) received the B.S. degree in electrical engineering from Xi'an Jiaotong University, Xi'an, China, in 1982, and the M.S. and Ph.D. degrees in electrical engineering from the University of Southern California, Los Angeles, CA, USA, in 1985 and 1990, respectively. From 1990 to 1992, he was a Research Scientist with the Electric Power Lab, University of Southern California. In 1992, he joined the GE Power Systems Engineering Department, Schenectady, NY, USA, as an Application Engineer. From 1994 to 2000, he was a Senior Product Development Engineer with GE Industrial Systems, Salem, VA, USA. From 2000 to 2001, he was the Manager of Electronic and Photonic Systems Technology Lab, GE Global Research Center, Schenectady, and Shanghai, China. In 2001, he joined the Center for Power Electronics Systems, Virginia Tech, Blacksburg, VA, as a Research Associate Professor and became an Associate Professor in 2004. From 2003 to 2009, he was the CPES Technical Director. Since 2009, he has been with the University of Tennessee, Knoxville, TN, USA, and Oak Ridge National Lab, Knoxville, as a Professor and the Condra Chair of Excellence of power electronics. He is the Founding Member and the Technical Director of the multi-university NSF/DOE Engineering Research Center for Ultra-wide-area Resilient Electric Energy Transmission Networks (CURENT) led by the University of Tennessee. His research interests include wide bandgap power electronics, and power electronics applications for transportation and electric grid. Dr. Wang is a Fellow of the U.S. National Academy of Inventors.

**Mohammed Olama** (Senior Member, IEEE) received the B.S. and M.S. (Hons.) degrees in electrical engineering from the University of Jordan, Amman, Jordan, in 1998 and 2001, respectively, and the Ph.D. degree from the Electrical Engineering and Computer Science Department, University of Tennessee, Knoxville, TN, USA, in 2007.

He is currently a Senior Research Scientist with the Computational Sciences and Engineering Division, Oak Ridge National Laboratory, Oak Ridge, TN. He is also an Adjunct Associate Professor with the EECS Department, University of Tennessee. He has more than 180 archival publications (including journals, conference proceedings, book chapters, and technical reports) in addition to numerous presentations at professional conferences and international symposia. His research interests include smart grid and smart buildings, smart grid communications and control, cyber-physical systems, complex systems, wireless communications, healthcare data analytics, machine learning, artificial intelligence, statistical signal processing, and discrete-event simulation.

**Ben Ollis** (Senior Member, IEEE) received the B.S. and M.S. degrees in electrical engineering from the University of Tennessee, Knoxville, TN, USA, in 2012 and 2014, respectively. He is currently an R&D Staff Member and a Power System Research Engineer with Oak Ridge National Laboratory, Oak Ridge, TN. Since 2013, he has been a Member of ORNLand also with the Grid Systems Architecture Group. He has utility experience as a planning Engineer with Duke Energy and as a Power System Operator with Clinton Utilities Board. He leads research projects focuses on small- and large-scale microgrids, networked microgrids, grid resiliency, device interoperability, and novel energy generation technologies.

**Maximiliano Ferrari** (Member, IEEE) received the B.S. degree in electrical engineering from the University of Javeriana, Bogotá, Colombia, and the second B.S. degree in physics from Allegheny College, Meadville, PA, USA, the M.S. degree in electrical engineering from the Polytechnic University of Valencia, Valencia, Spain, and the Ph.D. degree in energy science from the University of Tennessee-Knoxville, Knoxville, TN, USA. He currently with Grid Systems Architecture Group, Oak Ridge National Laboratory. His research interests include power electronics, microgrids controls and protection.